RSC Advances

PAPER

View Article Online
View Journal | View Issue

Check for updates

Cite this: *RSC Adv.*, 2020, **10**, 6640

High voltage vacuum-processed perovskite solar cells with organic semiconducting interlayers†

Azin Babaei, Chris Dreessen, Michele Sessolo * and Henk J. Bolink

In perovskite solar cells, the choice of appropriate transport layers and electrodes is of great importance to guarantee efficient charge transport and collection, minimizing recombination losses. The possibility to sequentially process multiple layers by vacuum methods offers a tool to explore the effects of different materials and their combinations on the performance of optoelectronic devices. In this work, the effect of introducing interlayers and altering the electrode work function has been evaluated in fully vacuum-deposited perovskite solar cells. We compared the performance of solar cells employing common electron buffer layers such as bathocuproine (BCP), with other injection materials used in organic light-emitting diodes, such as lithium quinolate (Liq), as well as their combination. Additionally, high voltage solar cells were obtained using low work function metal electrodes, although with compromised stability. Solar cells with enhanced photovoltage and stability under continuous operation were obtained using BCP and BCP/Liq interlayers, resulting in an efficiency of approximately 19%, which is remarkable for simple methylammonium lead iodide absorbers.

Received 8th January 2020
Accepted 4th February 2020

DOI: 10.1039/d0ra00214c

rsc.li/rsc-advances

Open Access Article. Published on 12 February 2020. Downloaded on 2/10/2026 6:59:19 AM.
This article is licensed under a Creative Commons Attribution-NonCommercial 3.0 Unported Licence.

1 Introduction

Organic–inorganic lead halide perovskites are being widely studied in thin-film optoelectronics and especially photovoltaics,[1] in view of their good semiconducting properties.[2] They typically exhibit a high absorption coefficient, long carrier diffusion length, high tolerance to chemical defects, and they can be prepared as high quality thin-films through a variety of deposition techniques.[3] In particular, perovskite thin-films can be readily prepared by solution processing or vacuum methods at low temperature, which is desirable when scaling up the device fabrication.[4,5] In perovskite solar cells, the photogenerated charge carriers need to be efficiently and selectively transported to the electrodes, minimizing non-radiative charge recombination. For this reason, the perovskite film is typically sandwiched in between organic or inorganic semiconductors, acting as electron and hole transport layers (ETL and HTL, respectively).[6] Several studies have been focused on the understanding of charge transfer and interfacial processes between the perovskite, the ETLs, and the electrode, with the ultimate goal of maintaining a high charge collection efficiency and to abate non-radiative charge recombination.[7] Among ETLs, notable examples are n-type metal oxides,[8] in particular TiO_2 and SnO_2, while the most widely adopted organic semiconductors are fullerene derivatives.[9] Fullerenes cannot only selectively transport electrons between the perovskite and the electrode, but are also capable to effectively passivate trap states and mitigate ionic migration at the perovskite surface and at the grain boundaries.[10] Efficient electron extraction, ensuring high open-circuit voltage (V_{oc}) and fill factor (FF), requires matching of the lowest unoccupied molecular orbital (LUMO) of the fullerene with the electrode work function. In a first approximation, this can be simply attained by using low work function electrodes such as calcium or barium,[11,12] although stable metals (Ag, Au) can also lead to ohmic contacts with fullerenes due to the formation of interfacial dipoles.[13,14] Another approach to reduce the energy mismatch between a semiconductor and an electrode is to increase the charge-carrier density in the organic semiconductor through doping.[15–17] In p–i–n perovskite solar cells employing fullerene ETLs, typically C_{60} or 1-[3-(methoxycarbonyl)propyl]-1-phenyl-[6.6]C_{61} (PCBM), ohmic injection is ensured by depositing a thin interlayer between the ETL and the electrode. This includes different molecules such as 1,3,5-tri(*m*-pyrid-3-yl-phenyl)benzene (TmPyPB)[18] or (2-(1,10-phenanthrolin-3-yl)naphth-6-yl) diphenylphosphine oxide (DPO),[19] inorganic salts such as LiF,[20] or n-type metal oxides.[21,22] The most widely adopted interlayer is a thin (5–10 nm) film of 2,9-dimethyl-4,7-diphenyl-1,10-phenanthrolin (bathocuproine, BCP), which is sublimed onto C_{60} and covered with a silver or aluminium electrode. BCP is a wide band gap material with a deep highest occupied molecular orbital (HOMO, >6.5 eV) and shallow LUMO (3–3.5 eV, Fig. 1a), which makes it suitable as exciton-blocking layer in organic electronics.[23–27] By simply considering the flat band energy diagram in Fig. 1a, BCP would not appear as

Instituto de Ciencia Molecular, Universidad de Valencia, C/Beltrán 2, Paterna, 46980, Spain. E-mail: michele.sessolo@uv.es

† Electronic supplementary information (ESI) available. See DOI: 10.1039/d0ra00214c

This journal is © The Royal Society of Chemistry 2020

Open Access Article. Published on 12 February 2020. Downloaded on 2/10/2026 6:59:19 AM.
This article is licensed under a Creative Commons Attribution-NonCommercial 3.0 Unported Licence.

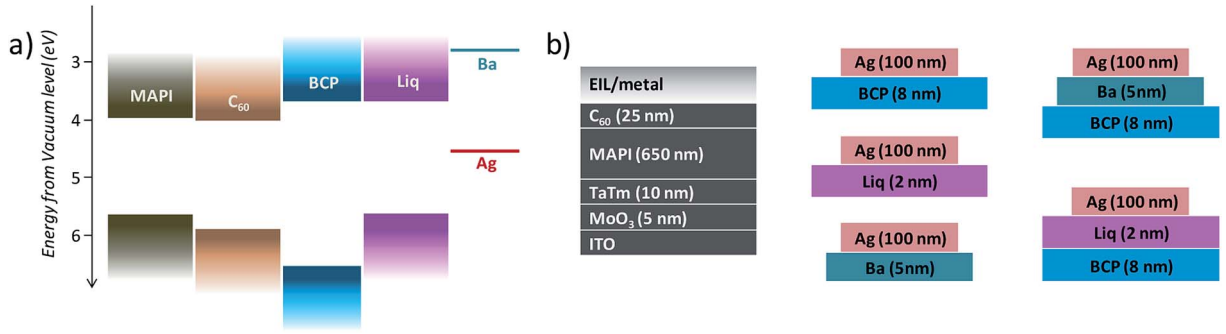

Fig. 1 (a) Flat band energy diagram of the materials used as electron transport/injection layers and electrodes. (b) Device schematics with thickness of all layers and highlight of the five different device structures studied in the paper.

a rational choice to match the energy levels of C_{60} and Ag, as its small electron affinity would hinder both the electron injection and extraction at the C_{60}/Ag interfaces. However, several reports have shown a strong chemical reaction occurring upon thermal vacuum deposition of Ag onto the BCP, and leading to the formation of Ag-BCP organometallic complexes.[24,28] These compounds would mediate charge transport due to the formation of new states well below the LUMO of pristine BCP, which justifies the efficient electron injection/extraction properties of BCP in optoelectronic devices.[25] This widely accepted view is challenged by recent reports where BCP was found to efficiently mediate electron transfer when placed in between an indium tin oxide (ITO) electrode and C_{60}, where the formation of organometallic species is unlikely.[29] In perovskite solar cells, non-radiative recombination is dominant at dislocations, grain boundaries, impurities as well as at the contact interface, and in all cases it unavoidably diminishes the attainable open-circuit voltage.[30] Non-radiative recombination in the perovskite layer can be regulated through controlled film crystallization/processing, while interface recombination should be minimized through the choice of suitable transport materials and optimized device architectures.[31] The influence of interlayer chemical and electronic properties on transport and recombination in vacuum-deposited perovskite solar cells has not been fully investigated, although it is critical to modulate and maximize FF, V_{oc} and stability. Here we studied the influence of interlayers and cathode work function at the C_{60} interface in vacuum-deposited p–i–n perovskite solar cells. In particular, we compared BCP with 8-hydroxyquinolinolato-lithium (Liq, Fig. 1a), a common electrode interlayer used in high efficiency organic light-emitting diodes (OLEDs).[32] Liq has HOMO and LUMO energies of −5.6 eV and −3.2 eV from the vacuum level, respectively,[33] and has the advantage of being easily processed by thermal evaporation or solution.[34,35] As for the case of BCP, the electron injection mechanism of Liq is not completely understood, but the most accepted hypothesis is that it is able to release metallic lithium upon reaction with the metallic cathode, leading to interfacial reduction of the underlying ETL.[36,37] In this work, we compared fully vacuum-deposited MAPI solar cells employing organic semiconductors as the transport and injection materials. We examined the influence of different thin electron injection layers and of the metal work function on the performance of p–i–n solar cells, where the electron transport layer is deposited on top of the perovskite and before the metal electrode. We compared the performance of the devices using BCP, Liq or combinations of them, using either Ag or Ba as the top electrode. We identified that while low work function metals can enhance the open-circuit voltage, they do it at the expense of the fill factor and especially of the stability. Using bare BCP or a combination of BCP and Liq led to solar cells with improved rectification, high photovoltage, and long-term stability.

2 Results and discussions

Details of preparation and characterization of materials and devices are reported in the experimental section. Briefly, we processed a 650 nm thick MAPI film and employed it in the fabrication of p–i–n perovskite solar cells. All layers were prepared by vacuum sublimation of the corresponding inorganic or organic materials in high-vacuum chambers. A scheme of the device structure is reported in Fig. 1a. A thin layer of molybdenum oxide (MoO_3, 5 nm) was deposited onto pre-patterned ITO-coated glass slides, acting as hole injection layer (HIL). As the HTL we used a 10 nm thick N^4,N^4,$N^{4\prime\prime}$,$N^{4\prime\prime}$-tetra([1,1′-biphenyl]-4-yl)-[1,1′:4′,1″-terphenyl]-4,4″-diamine (TaTm) film, while C_{60} was used in all cases as the ETL on top of the perovskite. We then finished the devices using 5 different variations of interlayers and metals (Fig. 1b), namely BCP (8 nm)/Ag, Liq (2 nm)/Ag, Ba (5 nm)/Ag, and the combinations BCP (8 nm)/Ba (5 nm)/Ag and BCP (8 nm)/Liq (2 nm)/Ag, where Ag is 100 nm thick in all cases. The latter two combinations were chosen to assess whether BCP can be used in combination with a low work function metal (Ba), or when not in contact with Ag (using a Liq interlayer). To ensure sufficient statistics, for each device configuration, at least 2 different substrates each containing 4 cells were evaluated, while for top performing configurations at least 5 different substrates with a total of 20 cells were characterized. The overlap area between the metal and ITO electrode was 6.51 mm^2 (2.1 × 3.1 mm^2) and the solar cell characteristics were measured under illumination with a 4 mm^2 mask to accurately determine the short circuit current (J_{sc}), and without a mask to avoid erroneous determination of both open-circuit voltage and fill factor.[38]

Open Access Article. Published on 12 February 2020. Downloaded on 2/10/2026 6:59:19 AM.
This article is licensed under a Creative Commons Attribution-NonCommercial 3.0 Unported Licence.

We initially tested the optoelectronic properties of the devices by measuring the current density–voltage (J–V) curves under AM 1.5G simulated sun illumination at the intensity of 100 mW cm^{-2} (Fig. 2a and Table 1). Very small and negligible differences were observed between forward (from short to open circuit) and reverse (from open to short circuit) scans. The lack of hysteresis in the J–V curves suggests that no charge accumulation takes places at the perovskite/transport layers' interface, indicating good energy level matching among the different materials. All solar cells were characterized by a similar J_{sc} of approximately 20.5 mA cm^{-2}, which is reasonable as all devices share the exact same stack of materials at the front contact, and the internal field is sufficient to overcome eventual energy barriers induced by the use of different ETLs. The internal reference device with BCP/Ag top contact delivered a high V_{oc} of 1.13 V with good rectification (FF of 77.6%), resulting in a PCE of 18.1% on average. When exchanging BCP for Liq, we observed that the photovoltaic parameters are essentially unvaried, leading to a V_{oc} of 1.13 V and a PCE of 18.1% on average. Devices employing BCP in combination with the low work function Ba electrode exhibited a low FF (67.1%) suggesting hindered charge extraction, despite of the ohmic BCP/Ba electron transport interface. Most likely, with this device structure the electron extraction is limited by the large potential difference between the LUMOs of C_{60} and BCP, and there is no beneficial interaction between BCP and Ba, as often reported for BCP in combination with Ag and Al. This is an additional indirect evidence that indeed metals such as Ag and Al do interact with BCP leading to the formation of new species and of an additional density of states below the BCP LUMO, as described above. The V_{oc} was also found to be slightly lower (1.11 V), and the overall efficiency was 15.7%. More interesting is the other device variation where we included Liq as interlayer between BCP and Ag. The diodes with BCP/Liq/Ag top contact exhibited a $V_{oc} = 1.12$ V, slightly higher compared to those with BCP/Ba, but with a much better rectification, as the FF approached 80% with small pixel-to-pixel variation. The latter observation might suggest that the chemical interaction between BCP and Ag takes place even in the presence of the Liq interlayer, due to its very low thickness (2 nm).

Finally, the solar cells employing the top Ba electrode deposited directly on the C_{60} ETL delivered the highest V_{oc} of 1.15 eV, even though at the price of a small decrease in FF. The observed trends in photovoltage were not related with the diode dark J–V characteristics (Fig. 2b), where all solar cells showed rather low and comparable leakage current in the low voltage regime. In this regime, the minimum of the current density for devices with Ba and Liq appeared at low negative voltage, indicating a small carrier accumulation within the device. Only devices finished with Ba were found to have a slightly higher

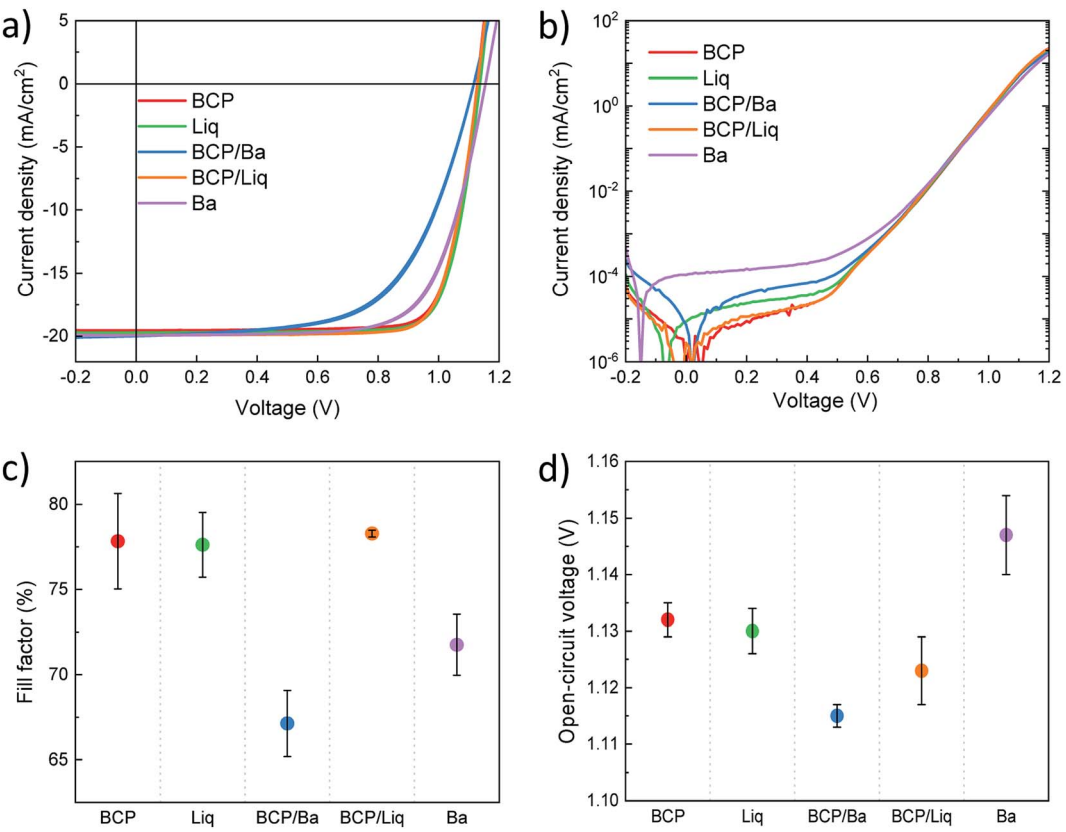

Fig. 2 (a) Representative J–V curves measured under simulated solar illumination in forward (short to open circuit) and reverse (open to short circuit) scan direction for each studied device. Due to the lack of hysteresis the two scans are indistinguishable. (b) J–V characteristics collected in the dark. Statistics on the (c) FF and (d) V_{oc} as a function of the top contact used.

 This journal is © The Royal Society of Chemistry 2020

Open Access Article. Published on 12 February 2020. Downloaded on 2/10/2026 6:59:19 AM.
This article is licensed under a Creative Commons Attribution-NonCommercial 3.0 Unported Licence.

leakage, but that is also not reflected in the measured V_{oc}, which was the highest across the entire device series.

While still a topic of debate, it is commonly accepted that a good energy level alignment is favourable for the carrier extraction (FF) and to limit recombination (increase V_{oc}) at the transport layer/perovskite interface.[7] In our case, however, the MAPI/ETL interface is unvaried, as in all device variations we have employed C_{60} in contact with the perovskite. One effect responsible for the difference in V_{oc} could be a variation of the diode built-in potential, which might help remove the majority carrier (electrons) from the MAPI/C_{60} interface. However, we did not observe appreciable differences in the built-in potential across the series of devices (Fig. S1†).

At open-circuit all photogenerated charge carriers recombine, and non-radiative recombination will reduce the quasi-Fermi-level splitting (QFLS), and hence limit the attainable photovoltage. As in perovskites recombination takes place from free charge carriers, the QFLS can be directly related to the perovskite photoluminescence quantum yield.[39] Hence, we performed photoluminescence (PL) measurements on full devices with the different top contacts. In order to compare the PL, we characterized the solar cells in an integrated sphere, illuminating the pixel with a 522 nm laser. We adjusted the laser power so that the J_{sc} of the cells matched the one obtained under simulated solar illumination, ensuring to have the same carrier concentration for all devices. All the PL spectra were taken with an integration time of 1 s.

The series of devices exhibited PL spectra with maxima centred at 1.58 eV (Fig. 3), independently on the top contact composition, but with different intensity. In general, V_{oc} fluctuations can be ascribed to a variation of the non-radiative recombination rates (change of the PL quantum yield) in the device. In particular, the more intense PL (and V_{oc}) observed for solar cells capped with Ba indicates that the electrode work function has indeed an important role on the charge carrier recombination dynamics of the perovskite film, even across the C_{60} film. On the other hand, devices with BCP and Liq showed the lowest PL intensity, while the combined BCP/Liq and BCP/Ba top contacts were found to lead to brighter PL. The solar cells with BCP and Liq interlayers were characterized by a high V_{oc}, although not accompanied by a proportionally intense PL signal, suggesting other competitive mechanisms determining the final photovoltage. It is important to note that the trends observed in the PL might be affected, at least partially, to transient phenomena which will be discussed below. The fact that both the electrode work function and type of interlayers can influence the MAPI PL, even when the adjacent C_{60} ETL is unvaried, reflects some of the unique properties of perovskites. It has been widely reported that the perovskite Fermi level can be drastically modulated by choosing the appropriate substrate.[31] In particular, p-type substrates (NiO_x, or MoO_3) impose a p-type character on the perovskite itself, and the same but opposite mechanism is true for n-type materials, such as metal oxides or low work function surfaces in general.[40,41] Within this perspective, we can reasonably envision that the Fermi level of the MAPI films is directly influenced also by the top surface (the top contacts studied here). The work function of these materials is, however, very difficult to probe as the interface is buried within the device.

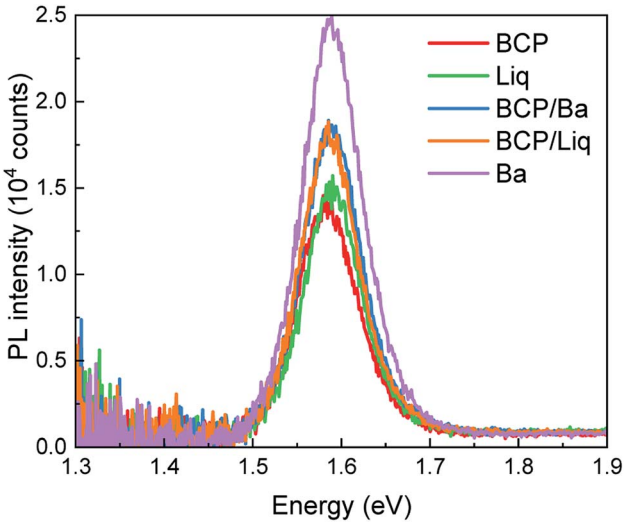

Fig. 3 Steady-state PL spectra of devices with different top contacts, excited with a 522 nm laser at the intensity equivalent to 1 sun illumination.

Table 1 Average photovoltaic parameters with standard deviation σ extracted from J–V curves for solar cells with different top contact

Top contact	FF (%)	V_{oc} (V) $\pm$ σ (mV)	J_{sc} (mA cm^{-2})	PCE (%)
BCP	77.8 $\pm$ 2.8	1.132 $\pm$ 3	20.5 $\pm$ 0.1	18.1 $\pm$ 0.2
Liq	77.6 $\pm$ 1.9	1.130 $\pm$ 4	20.4 $\pm$ 0.3	18.1 $\pm$ 0.3
BCP/Ba	67.1 $\pm$ 1.9	1.115 $\pm$ 2	20.7 $\pm$ 0.5	15.7 $\pm$ 0.1
BCP/Liq	78.3 $\pm$ 0.2	1.123 $\pm$ 6	20.6 $\pm$ 0.7	18.4 $\pm$ 0.2
Ba	71.8 $\pm$ 1.8	1.147 $\pm$ 7	20.7 $\pm$ 0.7	17.1 $\pm$ 0.6

We further investigated the characteristics of the series of solar cells by measuring their behaviour as a function of time, under continuous simulated solar illumination. The devices were encapsulated with UV-curable resin and a glass slide, and kept at 25 °C under a nitrogen flow (max relative humidity 10%), to minimize the effect of the environmental degradation. The maximum power point was continuously tracked and we also measured the device V_{oc} every 10 minutes. The evolution of the PCE over time for the series of devices are depicted in Fig. 4a. We can distinguish three types of behaviour for the device series. The solar cells employing Ba as the electrode (either alone or in combination with BCP) showed an initial fast rise in efficiency (to about 19%) followed by a relative fast decay of the device performance. After 2 days of continuous operation, the PCE for both devices was found to be already below 16%. This is expected as Ba is extremely reactive, and its implementation requires very rigorous encapsulation to ensure the absence of oxygen and/or moisture. On the contrary, the devices employing BCP and BCP/Liq in combination with the Ag electrode were found to be much more stable, and with rather similar decay profile. After 2 weeks of continuous operation, the device with BCP/Liq top contact still delivered a PCE of 15.5%, while the

Open Access Article. Published on 12 February 2020. Downloaded on 2/10/2026 6:59:19 AM.
This article is licensed under a Creative Commons Attribution-NonCommercial 3.0 Unported Licence.

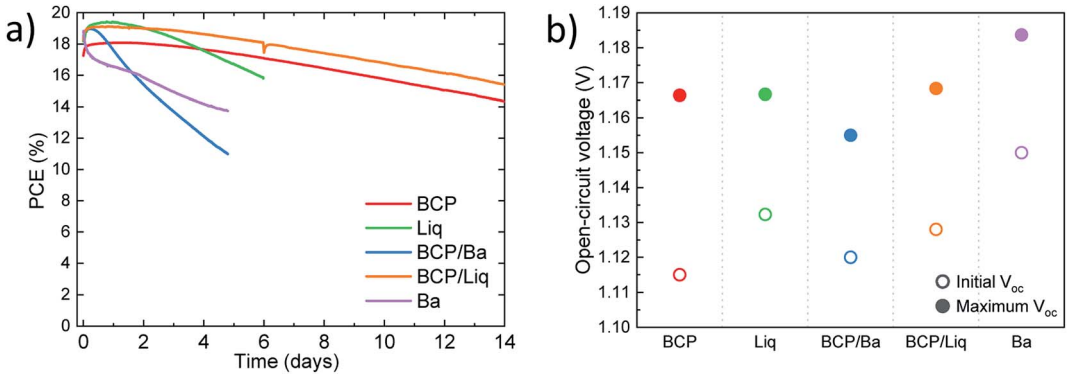

Fig. 4 (a) Evolution of the PCE of devices with different top contacts under continuous simulated solar illumination. (b) Open-circuit voltage for the same devices measured as-fabricated (empty symbols) and maximum V_{oc} recorded during maximum power point tracking (full symbols).

reference cell with only BCP showed an efficiency of 14.5%. Also in this set of devices we noted an initial rise of PCE to about 18% and 19% for cells with BCP and BCP/Liq top contacts, respectively.

The solar cell employing the thin Liq interlayer in between C_{60} and Ag showed a different behaviour, with an initial notable increase of the efficiency (up to 19.5% after 1 day) followed by a monotonic decay of the PCE, reaching about 16% after 6 days of operation. Apart from the perovskite intrinsic instability, the main processes driving the degradation of perovskite solar cells are the diffusion of halides to the electrode,[42] as well as the opposite migration of metal atoms from the electrode to the perovskite film.[43] With this in mind, we can reasonably ascribe the short lifetime observed for the cells with only 2 nm thick layers of Liq in between the C_{60} and Ag, to the faster interdiffusion of species between the MAPI film and the electrode. When BCP is used, it can alleviate this effect just because of the additional barrier it introduces, but likely also thanks to the ability of BCP to coordinate Ag atoms, as discussed above, which might slow down the metal diffusion. An interesting feature of the measurements under continuous illumination is the initial performance increase observed for the solar cells, independently on the top-contact used (although Ba was found to speed up the device degradation, as compared to the other interlayers). In particular, the open-circuit voltage was found to increase in all cases of about 40 to 50 mV, as illustrated in Fig. 4b. Considering that the variations are similar and virtually independent on the type of top-contact, their origin is most likely a consequence of a reduction of the non-radiative recombination within the MAPI film. A similar behaviour was previously observed in efficient vacuum-deposited n–i–p perovskite solar cells.[15] It has been widely reported that, under continuous illumination, the density of shallow traps can be reduced, leading to a decrease of the non-radiative recombination rate.[44,45] Interestingly, here we observed maximum V_{oc} close to 1.16 V for solar cells with BCP, Liq or their combinations, and up to 1.185 V for devices employing Ba as the electrode. Although in the latter case the stability was found to be very limited, these voltage values are among the highest reported for vacuum-processed MAPI solar cells.[15,46–48]

3 Conclusion

In summary, we have studied the influence of different interlayers, electrodes, and their combinations on the performance and especially the photovoltage of vacuum-processed perovskite solar cells. Organic semiconductors traditionally used in solar cells (BCP) and OLEDs (Liq) can lead to devices with high rectification, fill factor, and photovoltage. Furthermore, we have observed that the use of low work function metals, such as Ba, can be beneficial for the reduction of non-radiative recombination, although at the expenses of the device stability. Long-term device stability was observed only in the presence of BCP, with or without the Liq buffer layer. Future studies will address this aspect, trying to introduce low work function surfaces without undermining the device operation under continuous illumination.

4 Experimental section

4.1 Thin film and device preparation

To prepare the devices, the layers were deposited on ITO-coated glass substrates. The substrates were cleaned using soap, water, and subsequently isopropanol in an ultrasonic bath, followed by a UV-ozone treatment. The substrates were transferred into a nitrogen-filled glovebox (H_2O and O_2 < 0.1 ppm) equipped with a vacuum chamber with pressure lower than 10^{-6} mbar. MoO_3 and TaTm layers were deposited at rates of 0.1 and 0.4 Å s^{-1}, respectively. The MAPI films were deposited by co-evaporation of MAI and PbI_2 precursors simultaneously at the rates of 1.0 and 0.6 Å s^{-1}, respectively. The rates of the co-evaporation and the thickness of each layer were controlled by using three quartz crystal microbalance sensors. After deposition of the perovskite film, C_{60} was evaporated at a rate of 0.4 Å s^{-1} with the source temperature at 380 °C, and subsequently a thin layer (8 nm) of BCP was sublimed at a rate of 0.3 Å s^{-1} with a source temperature of 150 °C. Liq (2 nm) was deposited at a rate of 0.1 Å s^{-1}. Ba (5 nm) and Ag (100 nm) were evaporated in another vacuum chamber using molybdenum boats as sources by applying a current of 1 A and 3–4 A, respectively.

 This journal is © The Royal Society of Chemistry 2020

Open Access Article. Published on 12 February 2020. Downloaded on 2/10/2026 6:59:19 AM.
This article is licensed under a Creative Commons Attribution-NonCommercial 3.0 Unported Licence.

4.2 Device characterization

The *J–V* curves for the solar cells were recorded using a Keithley 2612A SourceMeter in a −0.2 and 1.2 V voltage range, with 0.01 V steps and integrating the signal for 20 ms after a 10 ms delay, corresponding to a speed of about 0.3 V s^{-1}. The devices were illuminated under a Wavelabs Sinus 70 LED solar simulator. The light intensity was calibrated before every measurement using a calibrated Si reference diode. Solar cell stability measurements (photovoltaic parameters *versus* time) were recorded using a maximum power point tracker system, with a white LED light source under 1 sun equivalent, developed by candlelight. During the stability measurements, the encapsulated devices were exposed to a flow of N_2 gas; temperature was stabilized at 300 K during the entire measurement using a water-circulating cooling system controlled by a Peltier element; *J–V* curve measurements were performed every 10 min.

4.3 Photoluminescence measurements

The photoluminescence of the full devices was measured with an Avantes AvaSphere-50-REFL integrating sphere connected to a 600 nm long-pass filter and an Avantes Avaspec2048 spectrometer. The devices were illuminated with a diode laser of integrated optics, emitting at 522 nm. The laser power was adjusted so that the short-circuit current *via* laser illumination matched the short-circuit current obtained from the measurement with the solar simulator. All the spectra were taken with an integration time of 1 s.

Conflicts of interest

There are no conflicts to declare.

Acknowledgements

The research leading to these results has received funding from the European Union Programme for Research and Innovation Horizon 2020 (2014–2020) under grant agreement No. 763977 of the PerTPV project, grant agreement No. 83441 of the ERC grant HELD, and from the Spanish Ministry of Economy and Competitiveness (MINECO) *via* the Unidad de Excelencia María de Maeztu MDM-2015-0538, MAT2017-88821-R, RTI2018-095362-A-I00, PCIN-2015-255, PCIN-2017-014, and the Generalitat Valenciana (Prometeo/2016/135). The project that gave rise to these results received the support of a fellowship from "la Caixa" Foundation (ID 100010434). The fellowship code is LCF/BQ/DI19/11730020. M. S. acknowledges the MINECO for his RyC contract.

References

1 A. K. Jena, A. Kulkarni and T. Miyasaka, *Chem. Rev.*, 2019, **119**, 3036–3103.
2 T. M. Brenner, D. A. Egger, L. Kronik, G. Hodes and D. Cahen, *Nat. Rev. Mater.*, 2016, **1**, 15007.
3 W. A. Dunlap-Shohl, Y. Zhou, N. P. Padture and D. B. Mitzi, *Chem. Rev.*, 2019, **119**, 3193–3295.
4 Z. Li, T. R. Klein, D. H. Kim, M. Yang, J. J. Berry, M. F. A. M. van Hest and K. Zhu, *Nat. Rev. Mater.*, 2018, **3**, 18017.
5 J. Ávila, C. Momblona, P. P. Boix, M. Sessolo and H. J. Bolink, *Joule*, 2017, **1**, 431–442.
6 H. D. Pham, L. Xianqiang, W. Li, S. Manzhos, A. K. K. Kyaw and P. Sonar, *Energy Environ. Sci.*, 2019, **12**, 1177–1209.
7 C. M. Wolff, P. Caprioglio, M. Stolterfoht and D. Neher, *Adv. Mater.*, 2019, 1902762.
8 S. S. Shin, S. J. Lee and S. Il Seok, *Adv. Funct. Mater.*, 2019, 1900455.
9 E. Castro, J. Murillo, O. Fernandez-Delgado and L. Echegoyen, *J. Mater. Chem. C*, 2018, **6**, 2635–2651.
10 Y. Shao, Z. Xiao, C. Bi, Y. Yuan and J. Huang, *Nat. Commun.*, 2014, **5**, 5784.
11 S.-Y. Hsiao, H.-L. Lin, W.-H. Lee, W.-L. Tsai, K.-M. Chiang, W.-Y. Liao, C.-Z. Ren-Wu, C.-Y. Chen and H.-W. Lin, *Adv. Mater.*, 2016, **28**, 7013–7019.
12 L. Gil-Escrig, C. Momblona, M. Sessolo and H. J. Bolink, *J. Mater. Chem. A*, 2016, **4**, 3667–3672.
13 S. C. Veenstra, A. Heeres, G. Hadziioannou, G. A. Sawatzky and H. T. Jonkman, *Appl. Phys. A: Mater. Sci. Process.*, 2002, **75**, 661–666.
14 O. Malinkiewicz, A. Yella, Y. H. Lee, G. M. Espallargas, M. Graetzel, M. K. Nazeeruddin and H. J. Bolink, *Nat. Photonics*, 2014, **8**, 128–132.
15 C. Momblona, L. Gil-Escrig, E. Bandiello, E. M. Hutter, M. Sessolo, K. Lederer, J. Blochwitz-Nimoth and H. J. Bolink, *Energy Environ. Sci.*, 2016, **9**, 3456–3463.
16 L. E. Polander, P. Pahner, M. Schwarze, M. Saalfrank, C. Koerner and K. Leo, *APL Mater.*, 2014, **2**, 081503.
17 T. H. Schloemer, J. A. Christians, J. M. Luther and A. Sellinger, *Chem. Sci.*, 2019, **10**, 1904–1935.
18 W.-H. Lee, C.-Y. Chen, C.-S. Li, S.-Y. Hsiao, W.-L. Tsai, M.-J. Huang, C.-H. Cheng, C.-I. Wu and H.-W. Lin, *Nano Energy*, 2017, **38**, 66–71.
19 K. Wang, M. Neophytou, E. Aydin, M. Wang, T. Laurent, G. T. Harrison, J. Liu, W. Liu, M. De Bastiani, J. I. Khan, T. D. Anthopoulos, F. Laquai and S. De Wolf, *Adv. Mater. Interfaces*, 2019, **6**, 1900434.
20 X. Liu, H. Yu, L. Yan, Q. Dong, Q. Wan, Y. Zhou, B. Song and Y. Li, *ACS Appl. Mater. Interfaces*, 2015, **7**, 6230–6237.
21 F. Fu, T. Feurer, T. P. Weiss, S. Pisoni, E. Avancini, C. Andres, S. Buecheler and A. N. Tiwari, *Nat. Energy*, 2017, **2**, 16190.
22 K. A. Bush, A. F. Palmstrom, Z. J. Yu, M. Boccard, R. Cheacharoen, J. P. Mailoa, D. P. McMeekin, R. L. Z. Hoye, C. D. Bailie, T. Leijtens, I. M. Peters, M. C. Minichetti, N. Rolston, R. Prasanna, S. Sofia, D. Harwood, W. Ma, F. Moghadam, H. J. Snaith, T. Buonassisi, Z. C. Holman, S. F. Bent and M. D. McGehee, *Nat. Energy*, 2017, **2**, 17009.
23 D. F. O'Brien, M. A. Baldo, M. E. Thompson and S. R. Forrest, *Appl. Phys. Lett.*, 1999, **74**, 442–444.
24 H. Gommans, B. Verreet, B. P. Rand, R. Muller, J. Poortmans, P. Heremans and J. Genoe, *Adv. Funct. Mater.*, 2008, **18**, 3686–3691.
25 H. Yoshida, *J. Phys. Chem. C*, 2015, **119**, 24459–24464.

Open Access Article. Published on 12 February 2020. Downloaded on 2/10/2026 6:59:19 AM.
This article is licensed under a Creative Commons Attribution-NonCommercial 3.0 Unported Licence.

26 J. Avila, L. Gil-Escrig, P. P. Boix, M. Sessolo, S. Albrecht and H. J. Bolink, *Sustainable Energy Fuels*, 2018, **2**, 2429–2434.
27 C. Chen, S. Zhang, S. Wu, W. Zhang, H. Zhu, Z. Xiong, Y. Zhang and W. Chen, *RSC Adv.*, 2017, **7**, 35819–35826.
28 M. Vogel, S. Doka, C. Breyer, M. C. Lux-Steiner and K. Fostiropoulos, *Appl. Phys. Lett.*, 2006, **89**, 163501.
29 F. Jafari, B. R. Patil, F. Mohtaram, A. L. F. Cauduro, H.-G. Rubahn, A. Behjat and M. Madsen, *Sci. Rep.*, 2019, **9**, 10422.
30 J. M. Ball and A. Petrozza, *Nat. Energy*, 2016, **1**, 16149.
31 P. Schulz, D. Cahen and A. Kahn, *Chem. Rev.*, 2019, **119**, 3349–3417.
32 J. Lee, H.-F. Chen, T. Batagoda, C. Coburn, P. I. Djurovich, M. E. Thompson and S. R. Forrest, *Nat. Mater.*, 2016, **15**, 92–98.
33 C. Schmitz, H.-W. Schmidt and M. Thelakkat, *Chem. Mater.*, 2000, **12**, 3012–3019.
34 T. Chiba, Y.-J. Pu, M. Hirasawa, A. Masuhara, H. Sasabe and J. Kido, *ACS Appl. Mater. Interfaces*, 2012, **4**, 6104–6108.
35 H. Kaji, H. Suzuki, T. Fukushima, K. Shizu, K. Suzuki, S. Kubo, T. Komino, H. Oiwa, F. Suzuki, A. Wakamiya, Y. Murata and C. Adachi, *Nat. Commun.*, 2015, **6**, 1–8.
36 J. Kido and T. Matsumoto, *Appl. Phys. Lett.*, 1998, **73**, 2866–2868.
37 F. A. Angel, R. Gao, J. U. Wallace and C. W. Tang, *Org. Electron.*, 2018, **59**, 220–223.
38 D. Kiermasch, L. Gil-Escrig, H. J. Bolink and K. Tvingstedt, *Joule*, 2019, **3**, 16–26.
39 R. T. Ross, *J. Chem. Phys.*, 1967, **46**, 4590–4593.
40 P. Schulz, L. L. Whittaker-Brooks, B. A. MacLeod, D. C. Olson, Y.-L. Loo and A. Kahn, *Adv. Mater. Interfaces*, 2015, **2**, 1400532.
41 S. Olthof and K. Meerholz, *Sci. Rep.*, 2017, **7**, 40267.
42 C. C. Boyd, R. Cheacharoen, T. Leijtens and M. D. McGehee, *Chem. Rev.*, 2019, **119**, 3418–3451.
43 C. C. Boyd, R. Cheacharoen, K. A. Bush, R. Prasanna, T. Leijtens and M. D. McGehee, *ACS Energy Lett.*, 2018, **3**, 1772–1778.
44 S. Chen, X. Wen, S. Huang, F. Huang, Y.-B. Cheng, M. Green and A. Ho-Baillie, *Sol. RRL*, 2017, **1**, 1600001.
45 R. Brenes, D. Guo, A. Osherov, N. K. Noel, C. Eames, E. M. Hutter, S. K. Pathak, F. Niroui, R. H. Friend, M. S. Islam, H. J. Snaith, V. Bulović, T. J. Savenije and S. D. Stranks, *Joule*, 2017, **1**, 155–167.
46 D. Pérez-del-Rey, P. P. Boix, M. Sessolo, A. Hadipour and H. J. Bolink, *J. Phys. Chem. Lett.*, 2018, **9**, 1041–1046.
47 V. S. Chirvony, K. S. Sekerbayev, D. Pérez-del-Rey, J. P. Martínez-Pastor, F. Palazon, P. P. Boix, T. I. Taurbayev, M. Sessolo and H. J. Bolink, *J. Phys. Chem. Lett.*, 2019, **10**, 5167–5172.
48 A. Al-Ashouri, A. Magomedov, M. Roß, M. Jošt, M. Talaikis, G. Chistiakova, T. Bertram, J. A. Márquez, E. Köhnen, E. Kasparavičius, S. Levcenco, L. Gil-Escrig, C. J. Hages, R. Schlatmann, B. Rech, T. Malinauskas, T. Unold, C. A. Kaufmann, L. Korte, G. Niaura, V. Getautis and S. Albrecht, *Energy Environ. Sci.*, 2019, **12**, 3356–3369.

 This journal is © The Royal Society of Chemistry 2020